

Magnetic levitation and spatial superposition of a nanodiamond with a current-carrying chip

Qian Xiang,¹ Shafaq Gulzar Elahi,² Andrew Geraci,² Sougato Bose,³ and Anupam Mazumdar¹

¹*Van Swinderen Institute, University of Groningen, 9747 AG Groningen, The Netherlands.*

²*Center for Fundamental Physics, Department of Physics and Astronomy, Northwestern University, 2145 Sheridan Road, Evanston, IL.*

³*Department of Physics and Astronomy, University College London, Gower Street, WC1E 6BT London, United Kingdom.*

(Dated: January 13, 2026)

We propose a current-carrying-chip scheme for generating spatial quantum superpositions using a levitating nanodiamond with a built-in nitrogen-vacancy (NV) centre defect. Our setup is quite versatile and we aim to create the superposition for a mass range of $10^{-19} \text{ kg} < m < 10^{-15} \text{ kg}$ and a superposition size $\mathcal{O}(10)\mu\text{m} < \Delta x < \mathcal{O}(1)\text{nm}$, respectively, in $t \leq 0.1\text{s}$, depending on the position we launch from the center of the diamagnetic trap. We provide an in-depth analysis of two parallel chips that can create levitation and spatial superposition along the x -axis, while producing a very tight trap in the y direction, and the direction of gravity, i.e., the z direction. Numerical simulations demonstrate that our setup can create a one-dimensional spatial superposition state along the x -axis. Throughout this process, the particle is stably levitated in the z -direction, and its motion is effectively confined in the y -direction for a Gaussian initial condition. This setup presents a viable platform for a diamagnetically levitated nanoparticle for a table-top experiment exploring the possibility of creating a macroscopic Schrödinger Cat state to test the quantum gravity induced entanglement of masses (QGEM) protocol.

1. INTRODUCTION

The quest to understand the quantum nature of gravity in a lab is a monumental challenge at the interface of theoretical physics and experimental science [1, 2], see also [3]. There are beliefs that gravity could be entirely classical, or that the wavefunction of a macroscopic object collapses due to gravity or other Standard Model interactions; see [4–8]. However, a promising avenue now exists to test such a hypothesis, which is known as the Quantum Gravity-induced Entanglement of Masses (QGEM) protocol [1, 9, 10]. The heart of the protocol lies with the fact that any quantum interactions will lead to entanglement, and if gravitational interactions with matter are quantum, then it must yield quantum entanglement between the two quantum objects mediated via a graviton exchange [1, 9, 10], see also [11–13]. The QGEM protocol can test alternative theories of gravity that have infinite derivatives and are ghost-free [14], massive graviton [15], test the quantum weak equivalence principle [16, 17], post-Newtonian theories of gravity [18], fifth force [19], and confirm the spin-2 nature of the massless graviton in the analogue light-bending due to gravity experiment via witnessing the entanglement between matter-and-photon [20].

However, the biggest challenge is to perform an experiment that creates a macroscopic quantum superposition in a lab, see [1]. To test QGEM, we will need to create a superposition of order $\Delta x \sim \mathcal{O}(10 - 50)\mu\text{m}$ for masses $m \sim 10^{-15} - 10^{-14}\text{kg}$ depending on the various rates of decoherence [1, 21, 22] and the witness, see [23–25].

This paper aims to develop a dedicated chip design that enables spatial superposition on a diamagnetically levitating platform, similar to [26], but now with on-chip superposition. This paper aims to provide a simple de-

sign for the matter-wave interferometer for a diamagnetic nanoparticle, such as a nanodiamond with a single nitrogen vacancy (NV) centre, plays an important role in creating macroscopic quantum superposition, as envisaged in [1, 27–35]. All these protocols exploit creating spatial superposition via the Stern-Gerlach interferometer (SGI) [36–41], which utilises a magnetic field gradient to couple the particle’s internal spin state to its center of mass (c.o.m) motional degrees of freedom. This coupling drives the particle’s c.o.m into a spatial superposition along a specific direction, effectively “splitting” its wavefunction. Current matter-wave interferometers have successfully implemented SGI configuration on atom chip protocols, see [39, 40, 42]. Following the methodology of atom chips, see [43], a scheme for creating spatial superpositions of more massive objects ($\sim 10^6$ carbon atoms) has been proposed in [40]. The pursuit of the next generation of SGI for higher mass is currently under extensive theoretical and numerical investigation, see [1, 27–35].

Recently, a blueprint for chip design has been proposed to trap nanodiamonds diamagnetically [44]. The new aspect of the chip was that the authors not only created a trap to suppress the nanodiamond’s motion, but also a long diamagnetic trap that enabled spatial superposition, as first envisaged in [24]. However, the current paper’s emphasis differs slightly; here, we focus solely on a current-carrying chip design solely to achieve Schrödinger Cat state. We will need another chip device to trap and cool the nanoparticle. However, our setup may be useful in hybrid scenarios, where cooling can be performed in an ion trap (e.g., a Paul trap [45–48]), while in a diamagnetic magnetic trap, we create a spatial superposition. Such a paradigm is feasible and has recently been discussed in the literature, see [44, 49].

Our proposed setup comprises two integral compo-

nents. The levitation assembly consists of four wires parallel to the x -axis, generating a magnetic quadrupole field [50, 51] in the $y - z$ plane to levitate the particle in the z -axis (which is the direction of Earth's gravity). While the splitting assembly, which creates the spatial superposition, consists of four long wires parallel to the z -axis, it also produces another quadrupole field in the $x - y$ plane. Together, the two assemblies can confine the particle's y -motion throughout the experiment. These wires are grouped into pairs and printed on four separate chips, see Fig. 1.

A key advantage of this configuration is that it creates approximately harmonic potential wells in all three spatial directions. Consequently, during the creation of the spatial superposition, the wavepacket does not spread in the orthogonal directions of the superposition, and the motion of the c.o.m along each interferometric arm, a feature crucial for maintaining interferometric visibility.

Furthermore, with our chosen parameters, the particle's three-dimensional motional modes within the device are nearly decoupled. This enables precise control over the superposition dynamics, allowing us to tailor the interferometer sequence along the desired axis (x) while maintaining stability in the y and z directions. However, note that we assume the nanodiamond to be spherical and assume that the NV center is located near the centre of the sphere. We do not consider the rotation of the nanodiamond; in this paper, we just study the c.o.m motion. The rotation of the nanodiamond is very important, and it has been studied in [52–54] in the context of the SGI interferometer. We will integrate the effect of rotation in a subsequent paper dedicated to both motional and rotational degrees of freedom. Also, we note that within our chip design, we will not be able to create an extremely large spatial superposition for a heavy mass. We will be able to create a modest superposition size of $\Delta x \sim \mathcal{O}(10 - 20)\mu\text{m}$ for $m = 10^{-19}\text{kg}$, for $\Delta x \sim \mathcal{O}(100)\text{nm}$ for $m = 10^{-17}\text{kg}$, and $\Delta x \sim \mathcal{O}(1)\text{nm}$ for $m = 10^{-15}\text{kg}$ in $t \sim 0.1\text{s}$, in the most ideal situation without including various effects from the decoherence, and the rotation of the nanodiamond.

This paper is structured as follows. In Section 2, we discuss how to achieve levitation (in the z -direction), transverse confinement (in the y -direction), and the creation of a spatial superposition state (in the x -direction) for the diamond embedded with NV spin by utilising two quadrupole magnetic fields. Specifically, in subsection 3, we present how to generate the required magnetic fields using wires fabricated on a silicon wafer. In subsection B.1, we combine the device description to elaborate on the steps necessary for creating the spatial superposition state and ultimately realising matter-wave interference. The method for calculating the magnetic fields produced by this device, as well as the computation of the wave packet trajectories, are presented in Appendix A and B, respectively.

2. MODEL

We consider using a nanoscale diamond embedded with a nitrogen-vacancy (NV) center spin. When it interacts with the magnetic field in space, the Hamiltonian is given by [30–32],

$$H = \frac{p_x^2 + p_y^2 + p_z^2}{2m} - \frac{\chi_\rho m}{2\mu_0} \mathbf{B}^2 + \hbar\gamma_e \hat{\mathbf{S}} \cdot \mathbf{B} + \hbar D \hat{S}_x^2 + mg\mathbf{z} \quad (1)$$

where the first term is the kinematic energy of the diamond whose mass is m . The second term represents the diamagnetic property of the nanodiamond, where $\chi_\rho \approx -6.2 \times 10^{-9} \text{ m}^3/\text{kg}$ [55], and $\mu_0 \approx 1.3 \times 10^{-6} \text{ T}\cdot\text{m}/\text{A}$ [56] are the mass magnetic susceptibility and the vacuum permeability, respectively. The third term is the key to achieving the separation of the nanodiamond wavepacket. It describes the interaction between the NV-center spin and the external magnetic field, where $\gamma_e \approx -1.8 \times 10^{11} \text{ rad}/(\text{s}\cdot\text{T})$ [56] is the electronic gyromagnetic ratio and $\hbar \approx 1.05 \times 10^{-34} \text{ J}\cdot\text{s}$ is the reduced Planck constant. $\hbar D \hat{S}_x^2$ is the NV zero-field splitting, where $D = 2.8 \text{ GHz}$. We will consider applying a sufficiently large bias magnetic field B_0 along the x -axis to ensure that the electronic spin of the NV-center remains parallel to the x -axis throughout the entire experimental process. The last term represents the gravitational potential energy of the levitated nanodiamond, where the gravitational acceleration constant $g \approx 9.8 \text{ m/s}^2$ is taken.

We consider a tabletop scenario in which the diamagnetic material is levitated in the z direction to avoid unwanted noise signals (for potential acceleration noise, see [57–61]). To simultaneously realise the creation of a spatial superposition state and magnetic levitation, while avoiding interference between these two types of dynamics, one can consider the magnetic field \mathbf{B} in Eq. (1) as consisting of two parts,

$$\mathbf{B}_L(y, z) = \eta_L z \mathbf{e}_z - \eta_L y \mathbf{e}_y, \quad (2)$$

$$\mathbf{B}_S(x, y) = (\eta_S x + B_0) \mathbf{e}_x - \eta_S y \mathbf{e}_y. \quad (3)$$

The total magnetic field is then,

$$\begin{aligned} \mathbf{B} &= \mathbf{B}_L + \mathbf{B}_S \\ &= (\eta_S x + B_0) \mathbf{e}_x - (\eta_L + \eta_S) y \mathbf{e}_y + \eta_L z \mathbf{e}_z. \end{aligned} \quad (4)$$

Here, B_0 denotes a uniform bias field applied solely along the x -direction to ensure the $B_x S_x$ term dominates in the Zeeman interaction. This uniform bias magnetic field can be generated using devices such as Helmholtz coils [62], which is not depicted in Fig. 1. The parameters η_L and η_S represent magnetic field gradients (T/m). The value of η_S assumes three distinct values during different stages to satisfy the trajectory closure requirement: $-\eta_1$, η_1 , and $-\eta_2$, with $\eta_1 > 0$ and $\eta_2 > 0$. This part of the discussion is given in section 4.

The motion of the nanodiamond in the z - and y -directions will be governed mainly by the diamagnetic

and gravitational terms

$$-\dot{\mathbf{p}}_i = \nabla_i \left(\frac{\chi_\rho m}{2\mu_0} \mathbf{B}^2 + mg\mathbf{z} \right), \quad (5)$$

where i represent y or z directions, respectively, and $\nabla_i = \partial_y \mathbf{e}_y + \partial_z \mathbf{e}_z$.

Consequently, in the y -direction, the overlap of two linear magnetic field components naturally forms a harmonic trap, with the equation of motion,

$$\frac{d^2y}{dt^2} + \omega_y^2 y = 0, \quad (6)$$

$$\omega_y = (\eta_L + \eta_S) \sqrt{\frac{-\chi_\rho}{\mu_0}}. \quad (7)$$

In an ideal situation, if the particle is initially positioned exactly at $y = 0$ with zero initial velocity, it will remain confined at $y = 0$. However, a Gaussian wavepacket will remain in a harmonic trap around $y = 0$, because as we shall see, the parameters enable us to create a very tight trap, or large ω_y . This behaviour can also be directly inferred from the form of the magnetic field given by Eqs. (2, 3) where the minimum of the total magnetic field in the y - z plane consistently lies along the axis at $y = 0, z = 0$. Consequently, the diamagnetic property of the particle will confine it to this region of minimum magnetic field. Substituting $y = 0$ into Eq. (2), it can be concluded that the y -component of the magnetic field $B_y(x, 0, z)$ experienced by the particle remains zero at all times.

Similarly, in the z direction, the equation of motion can be written as

$$-\frac{d^2z}{dt^2} = \omega_z^2 z + g \quad (8)$$

$$\omega_z = \eta_L \sqrt{\frac{-\chi_\rho}{\mu_0}} \quad (9)$$

During the derivation of the equation of motion Eq. (8), it can be observed that since \mathbf{B}_S does not contain a z -component, it does not contribute to the levitation effect. Therefore, from a functional perspective, the levitation of the particle is solely provided by \mathbf{B}_L , while its motion along the x -direction and the subsequent c.o.m separation induced by the spin-magnetic field coupling are exclusively governed by \mathbf{B}_S (discussed in section 4). In the z -direction, both magnetic fields jointly contribute to forming a harmonic potential well that confines the particle at $z \neq 0$, or the Gaussian wavepacket in the z -direction remains Gaussian and peaked at a value $z = z_L$, as discussed below. Again, this direction is an equally tight trap with a large ω_z ¹.

In order to realise stable levitation, the right-hand-side terms of Eq. (8) must be set to zero. Thus, the levitation height can be written as,

$$z_L = -\frac{g}{\omega_z^2}, \quad (10)$$

where $z_L < 0$. Substitute z_L into Eq. (4), the z -component of the total magnetic field can be written as

$$B_z(x, y, z_L) = \frac{g\mu_0}{\chi_\rho \eta_L} \approx -2000 \times \frac{1}{\eta_L} \text{ (T)}. \quad (11)$$

From Eqs. (8-11), the following conclusions can be drawn: (1) Due to the influence of gravity, the nanoparticle will always be pulled down to the equilibrium position z_L ; (2) Because of the non-zero equilibrium position z_L , the nanoparticle will always experience a non-zero magnetic field component along the z -direction; (3) Moreover, the magnitude of this component is inversely proportional to the gradient of the magnetic field used for levitation, η_L . Recall that we aim to use a bias magnetic field B_0 parallel to the x -axis to ensure the spin remains predominantly aligned along this direction. Therefore, it is particularly crucial to ensure that $|B_x| = |B_0 + x\eta_S| \gg |B_z| = |z_L\eta_L|$ holds at all times. To guarantee this condition is always satisfied, one possible option is to provide a sufficiently large B_0 , while the other is to achieve a sufficiently large magnetic field gradient η_L in Eq. (11).

Up to this point, we have discussed the effects arising from the ideal magnetic field forms given by Eqs. (2, 3, 4), which confine the nanoparticle at $y = 0, z = z_L$. Next, we discuss how to generate such magnetic fields using the setup shown in Fig. 1.

3. I-CAT CHIP

The chip design, shown in Fig. 1, given that it is a current controlled Chip which aims at creating a Schrödinger cat, we call it an I-Cat Chip. It is designed primarily to achieve two purposes. The first is to use the four levitation wires to generate a quadrupole magnetic field $\mathbf{B}_L = \eta_L(z\mathbf{e}_z - y\mathbf{e}_y)$ along the x -axis in the y - z plane. The second purpose is to use the four separation wires to generate a second quadrupole magnetic field $\mathbf{B}_S = (x\eta_S + B_0)\mathbf{e}_x - y\eta_S\mathbf{e}_y$ in the x - y plane. Here, B_0 is the bias field, which can be provided, for example, by Helmholtz coils. Consequently, in the vacuum region between the two “H”-shaped structures, the total magnetic field produced by the device takes the form $\mathbf{B} = (x\eta_S + B_0)\mathbf{e}_x - y(\eta_S + \eta_L)\mathbf{e}_y + z\eta_L\mathbf{e}_z$.

The setup primarily consists of four wires parallel to the x -axis (represented by the blue wires in Fig. 1) and four wires parallel to the z -axis (represented by the yellow wires in Fig. 1). We envision that these wires are printed on a single “H”-shaped structure as shown in Fig. 1(a, b, c); two identical “H” structures arranged side-by-side as shown in Fig. 1 (main) constitute the required device.

¹ The x -direction is nearly a flat direction, where ω_x will be given by Eq. 16. For $m = 10^{-19} \text{ kg}$, the values we set up, $\eta_1 \approx 100 \text{ T/m}$ and $\eta_2 \sim 99.9 \text{ T/m}$ leads to $\omega_x \sim 10 \text{ Hz}$. As we will see below for our setup we will have $\eta_L \gg \eta_S$, and $\eta_L \sim 10^5 \text{ Hz}$, so, we get, $\omega_y \sim \omega_z \sim 10^5 \text{ Hz}$, showing the hierarchy in the trap frequencies.

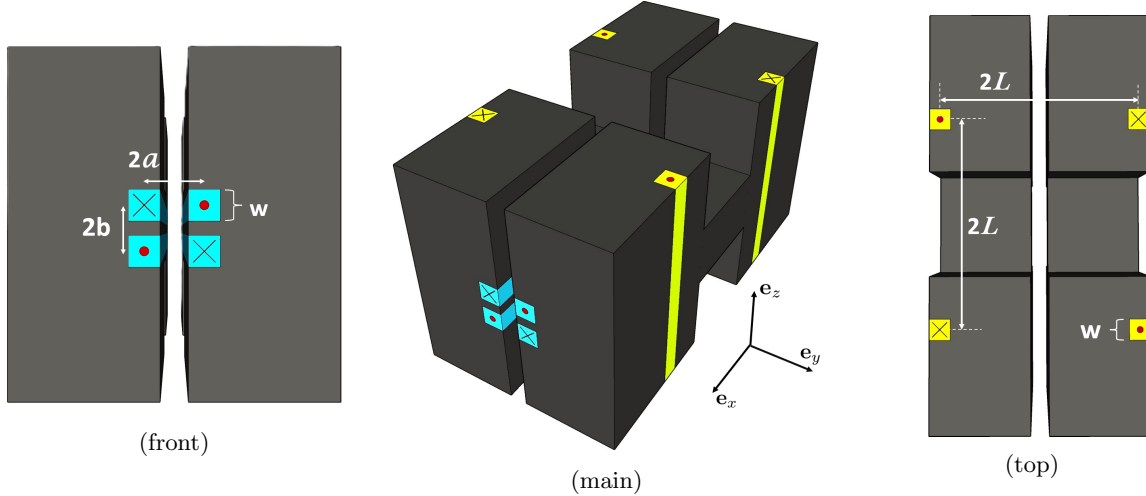


FIG. 1: Conception of the I-Cat chip design. In these diagrams (main, top and front views of the two chips), the black parts are Silicon wafers on which the wires are laid out. There are a total of four blue wires and four yellow wires on the carriers, which are made up of gold. According to their intended purposes, they are referred to here as levitation wires (blue) and separation (wave packet separation) wires (yellow), respectively. The coordinate system of the setup is defined at the geometric center of the entire device, where gravity is pointing in the negative z -direction, and the four levitation wires are parallel to the x -axis. These four wires are printed pairwise onto two “H”-shaped chips. The horizontal separation (spacing in the y -direction) between the two groups of levitation wires is denoted as $2a = 18\mu\text{m}$; the vertical separation (spacing in the z -direction) between the two levitation wires on the same chip is denoted as $2b = 14\mu\text{m}$.

Any two adjacent levitation wires carry currents of equal magnitude but opposite directions. A current flowing toward the positive x -direction is marked by a dot on the wire cross-section, while a current flowing toward the negative x -direction is marked by a cross on the cross-section (see also Tab. II in Appendix). The positively defined (according to the drawn coordinate system) current strength is denoted as $I_L = 24\text{A}$. Similarly, the four separation wires are printed pairwise onto two identical “H”-shaped structures and are parallel to the z -axis. The four separation wires form a square in the $x - y$ plane (see the top view in the first row)

with a side length of $2L$. Likewise, any two adjacent separation wires carry currents of equal magnitude but opposite directions. The positively defined current strength is denoted as $I = 10\text{A}$; a current flowing toward the positive z -direction is marked by a dot on the wire cross-section, while a current flowing toward the negative z -direction is marked by a cross on the cross-section (see also Tab. III in Appendix). We consider that every wire has the same width and thickness, denoted as $w = 10 \mu\text{m}$.

For the convenience of subsequent discussion, we define the origin of the coordinate system to be fixed at the geometric center of this symmetric setup, with the positive directions of \mathbf{e}_x , \mathbf{e}_y , and \mathbf{e}_z as indicated in Fig. 1 (main). We also define that currents flowing in the positive directions of \mathbf{e}_x and \mathbf{e}_z are considered positive, indicated by a red dot on the wire cross-section, while currents flowing in the directions of $-\mathbf{e}_x$ and $-\mathbf{e}_z$ are considered negative, indicated by a cross on the wire cross-section.

The levitation assembly, four blue wires form a rectangular configuration in the $y - z$ plane where the current flowing through them is the same in magnitude $|I_L|$ but opposite in direction for any two adjacent wires. The separation in the y -direction between the levitation wires located on the two “H” structures is $2a$; the vertical separation (spacing in the z -direction) between the levitation wires on the same “H” structure is $2b$. The nanodiamond, due to its diamagnetic property, will be confined within the vacuum region among these four levitation wires, which must extend sufficiently far in the

x -direction. This is because we aim to avoid magnetic field inhomogeneities introduced by the wire ends. Numerically, we consider the length of these wires to be $400 \mu\text{m}$. Due to the proximity of the diamond to the four levitation wires, we have modelled the width and thickness of the wires, here defined as equal in both dimensions, namely $w = 10 \mu\text{m}$. The purpose of these four levitation wires is to generate the magnetic field \mathbf{B}_L from Eq. (2) in the $y-z$ plane. In the region far from the wire ends, \mathbf{B}_L is independent of the x -coordinate and possesses only y - and z -components. Such a configuration could be fabricated by affixing two silicon wafer chips together with a spacer of thickness $2a - w \approx 8 \mu\text{m}$, and having each wafer of thickness of approximately $200 \mu\text{m}$ patterned with the required wire electrodes.

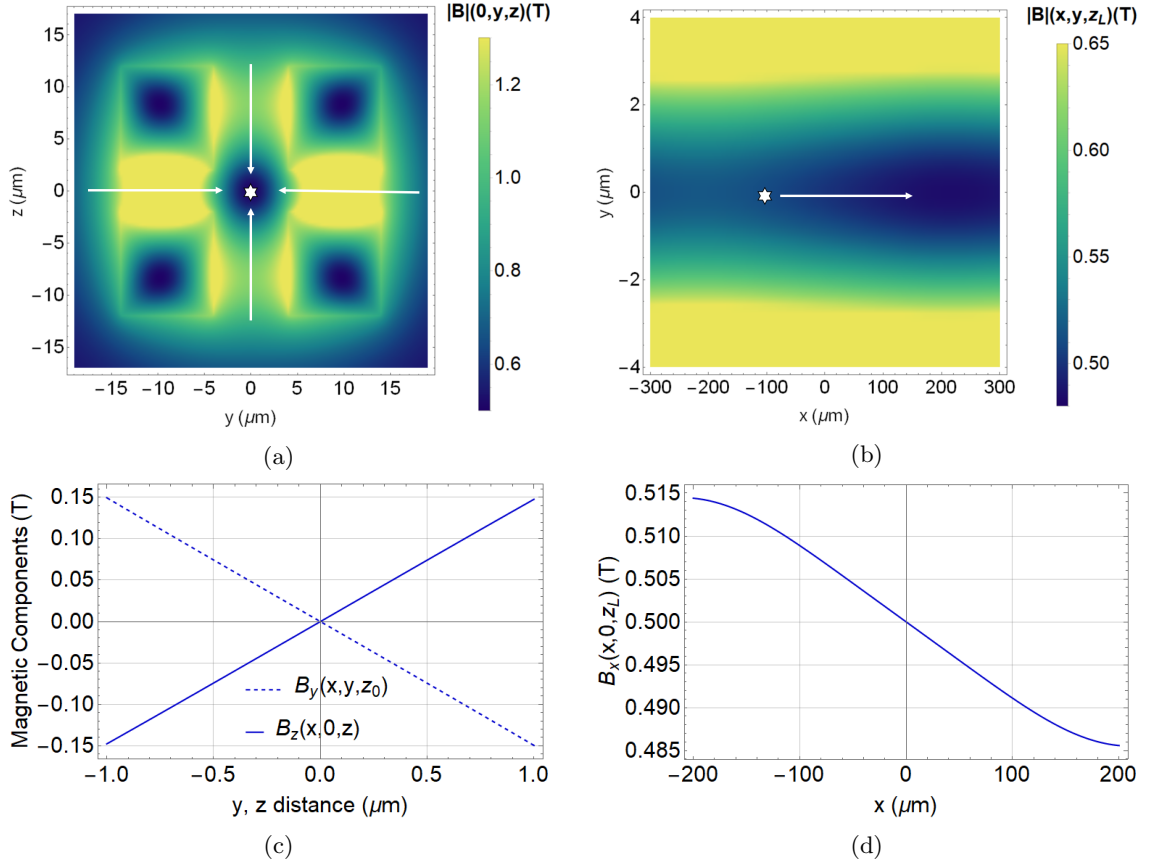


FIG. 2: Plots (a), (b), (c), and (d) present the results of the magnetic field and its components generated when both the separation assembly and levitation assembly are activated. Panels (a) and (b) display two-dimensional magnetic field magnitude distributions in the y - z and x - y planes, respectively. In panel (a), the parameters of the levitation wires ($2a = 18 \mu\text{m}$, $2b = 14 \mu\text{m}$, $w = 10 \mu\text{m}$, $I_L = 24 \text{ A}$) are consistent with those in Fig. 3. Here, we show a slice taken at $x = 0$. The result in (a) indicates that the diamagnetic force on the nanodiamond tends to confine the particle near $y = 0$, $z = 0$. Panel (b) illustrates the magnetic field at the slice $z = z_L$, where the field minimum occurs along the positive x -axis. The current magnitude $I = 10 \text{ A}$ and the geometric parameter of the separation assembly is $L = 200 \mu\text{m}$, the extension of four separation wires in the z -axis can be interpreted as infinitely long ($400 \mu\text{m}$ in numerical calculation). This implies that the diamagnetic force acts to push the nanoparticle toward the positive x -direction. It should be noted that before activating the separation assembly, the nanodiamond must be initialised at the position $(-x_0, 0, z_L)$. For the purpose of illustration, we take $x_0 = -100 \mu\text{m}$ in the panel (b), as shown by \star . We propose that this can be achieved using a device analogous to a “Z”-wire, which is not depicted in Fig. 1. Such a “Z”-wire structure would be positioned at the bottom of the setup, with its middle wire oriented perpendicular to the defined x -axis and fixed at $x = -x_0$, for details of Z-wire setup, see [44]. The levitation height during initialisation can be controlled by adjusting the magnitude of B_0 . A clear linear dependence can be observed in the vicinity of the region around $(0, 0, 0)$.

In order to support large currents in the wires ², gold

electrodes could be electroplated into trenches created by deep reactive ion etching in Silicon to allow efficient heat removal through the silicon, as was performed for the atom chip used in Ref. [63] for example.

² We estimate that within $t \sim 0.1 \text{ s}$, the heat generated by the conductor (which we assume to be Gold) is approximately $|I_L|R\Delta t^2 \approx 5.5 \text{ J}$, where $R = \rho_{\text{Au}} \cdot l/4ab$ is the electric resistance, $l = 400 \mu\text{m}$ is the length of levitation wires. Using a silicon wafer as a heat sink can effectively increase the current-carrying capacity of the conductor [63]. Furthermore, to prevent the silicon wafer from melting, it must be in contact with a cold source. Due to the millimetre-scale thermal diffusion length

In Fig. 2(a, b), we present the magnetic field gener-

in silicon over $t \sim 0.1 \text{ s}$, we get the diffusion length to be: $\sqrt{\alpha_{\text{Au}} \times 0.1} \approx 2.8 \text{ mm}$, where α_{Au} is the thermal diffusivity of bulk crystalline silicon at room temperature [64].

ated by the levitation assembly. The chosen parameters ³ are $2a = 18 \mu\text{m}$, $2b = 14 \mu\text{m}$, and $|I_L| = 24 \text{ A}$. From plots (a,b), it can be seen that the field minimum appears along the axis $(x, 0, 0)$, implying that the nanodiamond tends to be confined to this axis under the diamagnetic interaction. In regions sufficiently far from the wire ends, this configuration effectively forms a “guide rail” along which the diamagnetic particle undergoes guided motion ⁴. When gravity is accounted for, it pulls the equilibrium position of the particle downward, as can be seen from Fig. 3(c) ⁵. Thus, the particle is effectively confined along the axis $(x, 0, z_L)$, where z_L denotes the levitation height.

The relation between the magnetic field gradient produced by the levitation wires near their geometric central axis $(x, 0, 0)$ and geometric parameters a and b can be approximated as ⁶,

$$\eta_L = \frac{4\mu_0 I_L}{\pi} \frac{ab}{(a^2 + b^2)^2}. \quad (12)$$

The relation between the gradient η_L and the geometric parameters, i.e. a and b , is plotted in Fig. 4. In the plot, the vertical spacing is fixed at $2b = 14 \mu\text{m}$, gradients η_L produced by three sample currents, $|I_L| = 24, 18, 12 \text{ A}$, values versus horizontal distance $2a$ are shown in solid, dashed and dotted curves, respectively. The relation between the non-zero, $|B_z(x, y, z_L)| = |\eta_L z_L|$, component and the geometric parameter $2a$ is given in Fig. 5 where the vertical spacing is also fixed at $2b = 14 \mu\text{m}$ and the results given by $|I_L| = 24, 18, 12 \text{ A}$ are also shown. Recall that we aim to utilise a sufficiently large bias magnetic field B_0 parallel to the x -axis to ensure the spin

of the NV center remains predominantly aligned along the x -axis. This requires us to minimise $|B_z(x, y, z_L)|$ as much as possible. Therefore, from the results presented in Fig. 4 and 5, we can conclude that in order to reduce $|B_z(x, y, z_L)|$, one can either increase the levitation current $|I_L|$ or decrease the horizontal separation $2a$ between the levitation wires.

The four wires of the separation assembly are arranged on two “H”-shaped structures. The horizontal distance (spacing in the y -direction) between the two wires on different “H” structures is the same as the spacing between the two wires on the same “H” structure, which is $2L$. Here we choose $L = 200 \mu\text{m}$. Any two adjacent wires carry currents of equal magnitude $|I| = 10 \text{ A}$ but in opposite directions. Similar to the four wires of the levitation assembly, the purpose of the separation assembly is to generate the quadrupole magnetic field given by Eq. (3) in the $x - y$ plane. It is important to note that the bias magnetic field B_0 is an additional parameter; in practical experiments, one can consider using a set of Helmholtz coils to generate it.

In Fig. 2, we present the total magnetic field \mathbf{B} (plots (a), (b)) when both the levitation and the separation assemblies are activated, as well as its components (plots (c), (d)). Along the x -axis, examining the slice of the magnetic field in the $y-z$ plane (plot (a)), it can be observed that after incorporating the magnetic field \mathbf{B}_S generated by the separation assembly and the bias field $B_0 = 0.5 \text{ T}$, the minimum of $|B(0, y, z)|$ remains on the central axis of the device. This indicates that the diamond is still confined to the “guide rail” and can only move along it. In plot (b), viewing the variation of the total magnetic field in the (x, y) plane from above the positive z -direction, it is evident that in the y -direction, the magnetic field minimum is at $y = 0$. In the x -direction, the bias field B_0 shifts the minimum point of the magnetic field to $x \geq 300 \mu\text{m}$. Considering initialising the diamond particle at, for example, $x = -100 \mu\text{m}$, its diamagnetic property will drive it to move towards the positive x -direction. The electron in an NV centre is in a spin superposition state. Due to the spin-magnetic field coupling, the two states will experience different harmonic potential wells, thereby generating separation in their c.o.m motion, both in space and momentum. By adjusting the directions of the currents in the separation assembly, one can control the trajectories of the c.o.m to achieve a spatial superposition state and ultimately complete the one full-loop interferometer.

4. CREATING SUPERPOSITION

Here, we begin to discuss the specific details of generating the spatial superposition. First, recall that the function of the levitation assembly in Fig. 1 is to create strong harmonic potential wells in the y - and z -directions, confining the diamagnetic nanoparticle along the axis at $y = 0, z = z_L$. Along the x -direction, the separation

³ As a theoretical study, we have chosen smaller horizontal and vertical spacings along with a larger current, because such parameter settings can yield a significantly large magnetic field gradient η_L . This configuration can remarkably reduce the magnetic field’s z -component experienced by the nanoparticle, as given by Eq. (11), thereby allowing an additional bias field B_0 to be applied to ensure that the NV spin remains predominantly aligned along the x -axis.

⁴ With the device parameters I_L , $2a$ and $2b$, we effectively create a steep magnetic field gradient of $\eta_L \sim 10^5 \text{ T/m}$. From Eqs. (7, 9), it is evident that the particle is tightly trapped in both the y , z directions, with oscillation frequencies $\omega_y \approx \omega_z \sim \eta_L \sqrt{-\chi_\rho/\mu_0} = 1.05 \times 10^4 \text{ Hz}$. This is because $\eta_L \gg \eta_S$ for our parameters. Hence, for these parameters, $\Delta y \sim \Delta z = 10^{-29} \text{ m}$ for $m = 10^{-15} \text{ kg}$, while 10^{-27} m for $m = 10^{-19} \text{ kg}$. Note that the value of ω_y varies with the change of η_S (see section B for how η_S changes during a full-loop interferometry sequence). However, a small $|\eta_S| \approx 100 \text{ T/m}$ will not significantly alter the value of ω_y , since $\eta_L \sim 10^5 \text{ T/m}$. Consequently, such a design ensures that the creation of the superposition state is strictly one-dimensional, i.e. x -direction in our case.

⁵ $F_z(x, y, z)$ refers to diamagnetic repulsion $F_z(x, y, z) = -\partial_z \frac{-\chi_\rho m}{2\mu_0} \mathbf{B}^2(x, y, z)$.

⁶ This expression is derived from an infinitely long and thin model of conducting wire, details can be found in the Appendix A.1. Note that we use this expression only to simplify the discussion, while all subsequent numerical results will incorporate the actual width and thickness of the wires.

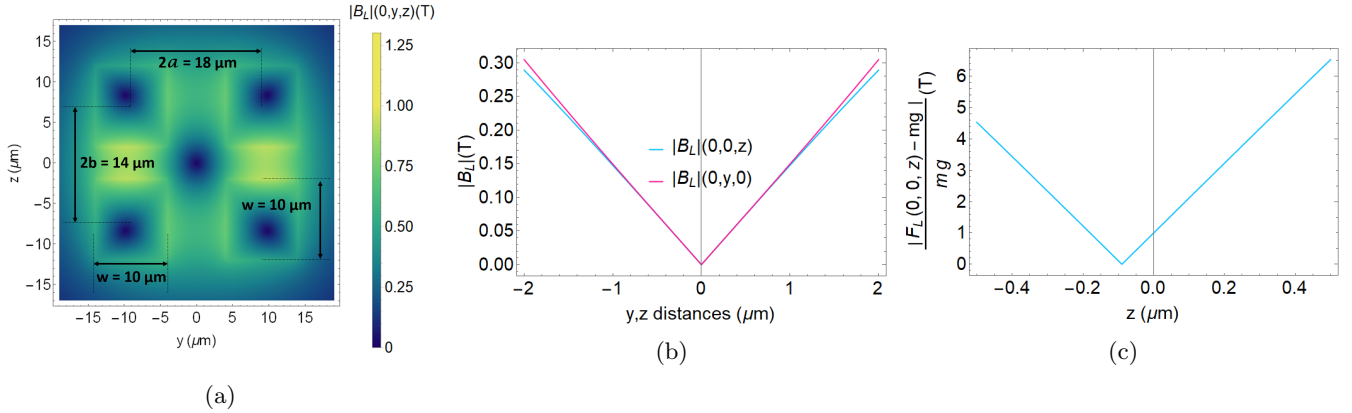


FIG. 3: Panels (a), (b), and (c) all present results generated by the levitation assembly shown in Fig. 1, displaying the magnetic field magnitude, field components, and levitation height, respectively. The square cross-sections in panel (a) indicate the positions of the four wires of the levitation assembly in the y - z plane, with horizontal and vertical separations of $2a = 18 \mu\text{m}$ and $2b = 14 \mu\text{m}$, respectively. The width and thickness of each wire is $w = 10 \mu\text{m}$, resulting in a minimum inter-wire spacing of $4 \mu\text{m}$. The current passing through the levitation assembly is $I_L = 24 \text{ A}$. As shown in panels (a) and (b), the levitation assembly creates two harmonic potential wells along the y - and z -directions. When gravitational effects are neglected, the diamagnetic property of the nanodiamond confines the particle to the axis at $y = 0, z = 0$. This axis corresponds to the shaded region (centre) in panel (a), where the magnetic field of the levitation assembly can be approximated by the form given in Eq. (2). Panel (c) shows that the particle's weight is balanced by the diamagnetic force, pulling the equilibrium levitation height downward. With our chosen parameters, the equilibrium height is $z_L \approx -0.0176 \mu\text{m}$.

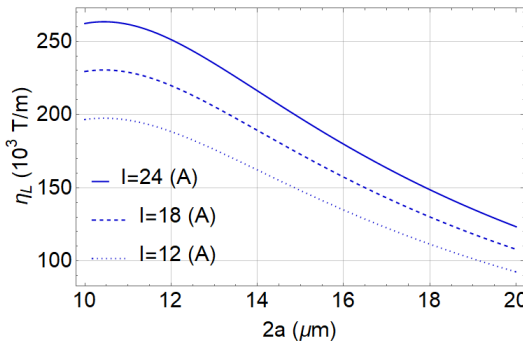


FIG. 4: The figure shows the relation between geometric parameter $2a$ (see Fig. 1 for its definition) and magnetic gradient η_L near the geometric centre of the assembly. The vertical spacing $2b = 14 \mu\text{m}$ is fixed. Curves represented by solid, dashed and dotted lines correspond to different levitation currents $I_L = 24, 18, 12 \text{ A}$, respectively.

assembly of the setup in Fig. 1 is responsible for creating a weaker harmonic potential. By varying both the magnitude and the direction of the currents I in the separation assembly, one can adjust both the magnitude of the magnetic gradient η_S and the direction of magnetic field along x axis. Specifically, to achieve the creation of the spatial superposition and the closure of the two trajectories, we consider \mathbf{B}_S of the following forms during

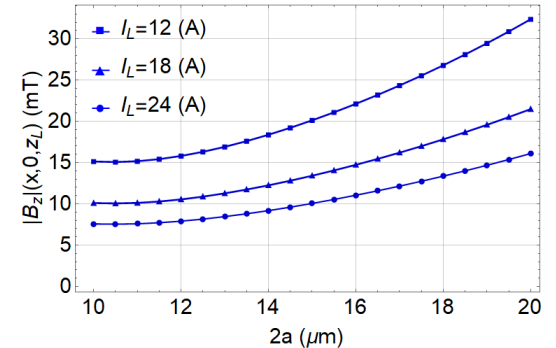


FIG. 5: The figure shows the relation between geometric parameter $2a$ (see Fig. 1) and magnetic field z component experienced by the nanodiamond when levitated.

different stages,

$$\mathbf{B}_S = \begin{cases} (B_0 - \eta_1 x) \mathbf{e}_x + \eta_1 y \mathbf{e}_y, & t \leq \tau_1 \\ (B_0 + \eta_1 x) \mathbf{e}_x - \eta_1 y \mathbf{e}_y, & \tau_1 \leq t \leq \tau_2 \\ (B_0 - \eta_2 x) \mathbf{e}_x + \eta_2 y \mathbf{e}_y, & \tau_2 \leq t \leq \tau_3 \end{cases} \quad (13)$$

$$\quad (14)$$

$$\quad (15)$$

where at different stages η_S takes different values, $\pm \eta_1$ and η_2 , where $\eta_1, \eta_2 > 0$ are defined. Such a magnetic field configuration is similar to [30, 34], where both utilise different magnetic fields (13), (14), (15) at different stages to control wave packet separation and recombination. Note that \mathbf{B}_S given above are also of ideal form, which we are aiming to generate by the separation

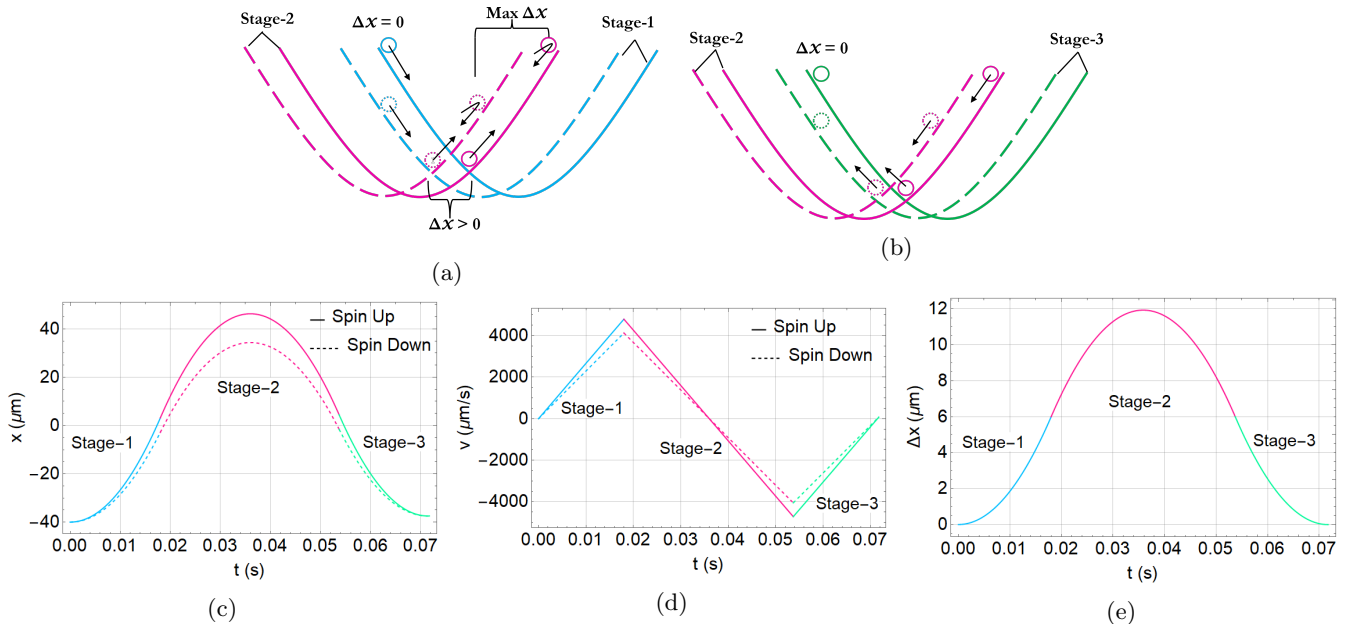


FIG. 6: Figures (c), (d), (e) illustrate the creation and recombination of the spatial superposition of a diamond with mass $m = 10^{-19}$ kg as an example. The solid and dashed lines represent the trajectories and velocities of the c.o.m for the spin-up and spin-down states, respectively. The process is divided into three stages, indicated by blue (stage-1), red (stage-2), and green (stage-3) curves. The current and geometric parameters of the levitation assembly remain unchanged across all stages and are identical to those in Fig. 2. In stage-1, the current in the separation assembly is set to $I = 10$ A, with a geometric parameter $L = 200$ μ m. The particle is initially positioned at $(-40, 0, z_L)$ with zero initial velocity. Under these conditions, the c.o.m exhibit no motion along the y - or z -directions. In stage-2, the current direction in each wire of the separation assembly is reversed, while the magnitude remains at 10 A. In stage-3, the currents' directions are reversed again, but the magnitude is slightly adjusted to 9.99 A to ensure closure of the c.o.m trajectories. Plots (a) and (b) depict the harmonic potentials experienced by the diamond particle during the three stages.

device. All subsequent results relating to the trajectories and velocities of wave packets are calculated by numerically simulated magnetic field. This part of the discussion is given in appendix A.1.

Note that, for the purpose of illustration, we will choose $m = 10^{-19}$ kg, spherical nanodiamond, and will provide the complete overhaul of the trajectories of the left and right parts of the interferometer, based on our chip design, see Fig. 6 of the trajectories of the two paths of the interferometer, and the illustrations of the potentials of the two two paths. For $m = 10^{-19}$ kg, shown in Fig. 6, we set $I = 10$ A for the separation wires, and the spacing between them is illustrated in Fig. 1, i.e., $L = 200$ μ m. With these conditions, we get $\eta_1 \approx 100$ T/m for stage-1 and -2. In Stage 3, to close the interferometer in both position and momentum space, the current in the separation wires is finely adjusted to $I = 9.99$ A. With these settings, the resulting gradient $\eta_2 \sim 99.9$ T/m. We will now perform an in-depth analysis of the protocol, as follows.

- **Preparation Stage:** Note that from the equations of motion, Eqs. (6, 8), regarding y and z direction, once the particle is well prepared at $(-x_0, 0, z_S)$

with its motional state sufficiently cooled, the harmonic trap will confine the diamond on this axis $y = 0$, $z = z_S$. This can be achieved by incorporating a “Z”-wire structure constructed in [44] beneath the setup shown in Fig. 1. This auxiliary structure would help load and levitate the nanodiamond to the height z_L , while enabling its initialisation at the position $y = 0$, $x = -x_0$ by adjusting the relative position between the “Z”-wire and the main device. While doing the motional state initialisation, the NV spin should also be prepared in the superposition state, $1/\sqrt{2}(|+1\rangle_x + |-1\rangle_x)$, and the NV axis must be predominantly aligned to the x -axis as well, due to the bias magnetic field B_0 . After the nanodiamond is prepared, the “Z”-wire is turned off, and we switch on the levitation assembly to capture the diamond. The levitation assembly remains active until the experiment concludes.

In the subsequent stages, the separation assembly will govern the motion of the nanodiamond along the x -direction, thereby reducing the dynamics to a one-dimensional model. The potential regarding

diamond's motion in the x direction can be written as,

$$U(S_x) = -\frac{\chi_\rho m}{2\mu_0} (B_0 + \eta_S x)^2 + \hbar\gamma_e S_x (B_0 + \eta_S x), \quad (16)$$

where in different stages, η_S , takes different values; $\pm\eta_1, \eta_2$ as shown in Eqs. (13,14,15). One should note that we employ the simplest linear form of \mathbf{B}_S here for the convenience of discussion. As can be observed from Fig. 2(d), as the nanodiamond moves away from the origin \mathbf{B}_S becomes less linear. Therefore, all subsequent results regarding the trajectories of the c.o.m are obtained from calculations using the numerically simulated magnetic fields, as detailed in the appendix B.

- **Stage-1:** During $t \in [0, \tau_1]$, Eq. (13) is relevant and the corresponding magnetic field. The equation of motion for spin up and down trajectories (along the x -direction) can be written as,

$$\frac{d^2x}{dt^2} = -\omega_1^2 x - \left(\frac{\chi_\rho B_0}{\mu_0} - \frac{\hbar\gamma_e S_x}{m} \right) \eta_1, \quad (17)$$

where $\omega_1 = \eta_1 \sqrt{-\chi_\rho/\mu_0}$ is the frequency in the first stage. As can be seen from Eq. (17), if the spin S_x were zero, the equation would reduce to a simple driven harmonic oscillator. However, due to the coupling between the spin superposition state and the magnetic field, the two c.o.m. experience different driving forces, leading to spatial separation during their motion. The solutions of Eq. (17) are,

$$x_1^\pm(t) = (-x_0 - k_1^\pm) \cos \omega_1 t + k_1^\pm \quad (18)$$

$$\dot{x}_1^\pm(t) = \omega_1(x_0 + k_1^\pm) \sin \omega_1 t, \quad (19)$$

where we define

$$k_1^\pm = k_1(S_x) = \frac{1}{\eta_1} \left(B_0 - \frac{\mu_0 \gamma_e \hbar S_x}{m \chi_\rho} \right). \quad (20)$$

Therefore, the two trajectories x^\pm correspond to spin up and down, respectively. As can be seen from the example shown in Fig. 6 (a), $-x_0 < 0$ is the initial position of stage-1 (blue curves), after released both wave packets will go to the positive side of x -axis. Alternatively, one can understand this from the perspective of the harmonic potential well given by Eq. (16). As illustrated in Fig. 6 (a), the particle initialised at position $x = -x_0$ effectively resides in two distinct potential wells due to the coupling between the NV spin and the magnetic field, with a difference in their potential energies. Consequently, as they move from the potential well toward the energy minimum point, the momentum difference gradually separates the spatial positions of the two c.o.m trajectories.

The choice of the initial position $-x_0$ actually offers considerable flexibility. Since in the first stage, we set $\eta_S = -\eta_1$ and $B_0 \gg |B_z(z_L)|$, the minimum of the magnetic field lies along the positive x -axis. Selecting a negative initial position thus allows one to fully utilise the “guide rail” space on both sides of the origin. One may also choose an initial point farther from the origin to increase the size of the spatial superposition state.

The duration of this stage, T_1 , can also be chosen with considerable flexibility. We opt to terminate this stage at the moment $\tau_1 = T_1$ when the trajectories of the two c.o.m reach the vicinity of $x = 0$.

$$\tau_1 = \frac{1}{\omega_1} \arccos \left(\frac{B_0}{\eta_1 x_0 + B_0} \right). \quad (21)$$

We will use τ_i and T_i for moments and durations of different stages. The physical meaning of the symbols used in this paper can be found in Tab. I.

TABLE I: Math symbols and physics interpretations.

Symbol	Meaning
ω_i	Frequencies corresponding to η_1 and η_2
x_i^\pm	Up and down trajectories of i -th stage.
X_i^\pm	Positions at the end of i -th stage.
\dot{X}_i^\pm	Velocities at the end of i -th stage.
T_i	Duration of i -th stage.
τ_i	Moment at the end of i -th stage ^a .

^aFor example, at the end of the first stage the duration is T_1 and the moment is $\tau_1 = T_1$, at the end of the second stage $\tau_2 = T_1 + T_2$.

- **Stage-2:** In the second stage, we map the magnetic field to the form given by Eq. (14), which corresponds to reversing the current direction in every wire of the separation assembly while keeping the current magnitude unchanged. At the beginning of this stage, as the magnetic field configuration changes, the c.o.m are placed into a new harmonic potential well (Fig. 6(a)). The potential energy experienced by the diamond along the x -direction, in the form, is still described by Eq. (16). Solutions of the second stage can be written as,

$$x_2^\pm(t) = (X_1^\pm + k_1^\pm) \cos [\omega_1(t - \tau_1)] - k_1^\pm + \frac{\dot{X}_1^\pm}{\omega_1} \sin [\omega_1(t - \tau_1)] \quad (22)$$

where $X_1^\pm = x^\pm(\tau_1)$ and $\dot{X}_1^\pm = \dot{x}^\pm|_{t=\tau_1}$ serve as the initial position and velocity in stage-2. Within this new potential well, the momenta of the c.o.m gradually decrease until they both reach the corresponding potential maxima. The superposition

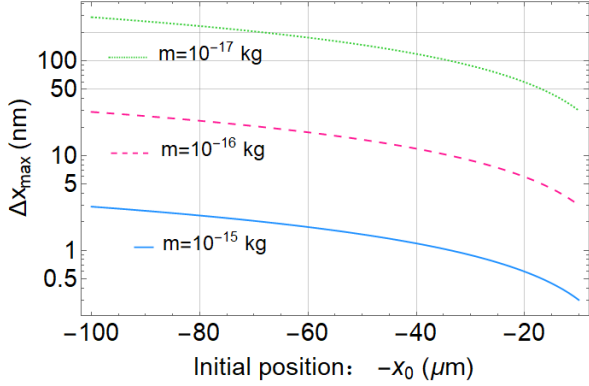


FIG. 7: The achievable maximum superposition size vs. initial position. We prepare the nanodiamond position $-x_0$, further away from the origin will cost more time for a full-loop. The total duration of the results shown here is $2t_{\max} \sim 0.1$ sec. The magnitude of gradient presents here for stage-1 and -2 are $\eta_1 \approx 100$ T/m, which correspond to $I = 10$ A and $2L = 200$ μm .

size, $\Delta x_2(t) = x_2^+(t) - x_2^-$ in this stage is then,

$$\begin{aligned} \Delta x_2(t) &= (\Delta X_1 + \Delta k_1) \cos [\omega_1(t - \tau_1)] - \Delta k_1 \\ &\quad + \frac{\Delta \dot{X}_1}{\omega_1} \sin [\omega_1(t - \tau_1)] \\ &= R \sin [\omega_1(t - \tau_1) + \phi] - \Delta k_1, \end{aligned} \quad (23)$$

where,

$$\begin{aligned} R &= \sqrt{\left(\frac{\Delta \dot{X}_1}{\omega_1}\right)^2 + (\Delta X_1 + \Delta k_1)^2} \\ \phi &= \arctan \left[\frac{\omega_1 (\Delta X_1 + \Delta k_1)}{\Delta \dot{X}_1} \right] \end{aligned} \quad (24)$$

and $\Delta X_1 = X_1^+ - X_1^-$, $\Delta \dot{X}_1 = \dot{X}_1^+ - \dot{X}_1^-$, $\Delta k_1 = k_1^+ - k_1^-$. At the moment,

$$t_{\max} = \frac{\pi - 2\phi}{2\omega_1} + \tau_1, \quad (25)$$

$\Delta x_2(t)$ in Eq. (54) reaches the maximum $\Delta x_{\max} = R - \Delta k_1$ which can be further expressed as,

$$\Delta x_{\max} = \Delta k_1 \left(\sqrt{\frac{B_0 + 5x_0\eta_1}{B_0 + x_0\eta_1}} - 1 \right). \quad (26)$$

where $-x_0$ is the initial position of the diamond in stage-1 (recall that we have defined x_0 as positive number), which implies that Δx_{\max} is mainly determined by this parameter. The relation of Δx_{\max} and initial position parameter x_0 is given in Fig. 7. As can be seen in the plot, releasing the diamond farther from the origin yields a larger superposition size. However, as the mass increases corresponding

superposition size is also reduced. This is because $\Delta k_1 = (k_1^+ - k_1^-) \propto 1/m$, as can be seen from Eq. (20).

After the moment t_{\max} , both wave packets start returning to $x = 0$. The timing for the determination of stage 2 also has considerable flexibility. Here, we simply choose the moment τ_2 when $x_2^\pm(\tau_2) = -X_1^\pm$.

- **Stage-3:** At this stage, \mathbf{B}_S is mapped to Eq. (15). Solutions at this stage are,

$$\begin{aligned} x_3^\pm(t) &= - (k_2^\pm - X_2^\pm) \cos [\omega_2(t - \tau_2)] \\ &\quad + k_2^\pm + \frac{\dot{X}_2^\pm}{\omega_2} \sin [\omega_2(t - \tau_2)] \end{aligned} \quad (27)$$

where, now the final state of positions X_2^\pm and velocities \dot{X}_2^\pm from stage-2 become the initials conditions for stage-3. likewise we define

$$k_2^\pm = k_2(S_x) = \frac{1}{\eta_2} \left(B_0 - \frac{\mu_0 \gamma_e \hbar S_x}{m \chi_\rho} \right).$$

Note that in this stage, the magnitude of magnetic gradient η_2 is different from η_1 . This is primarily because the linearity of the magnetic field \mathbf{B}_S generated by the separation assembly is imperfect, as can be observed in Fig. 2(d). The magnetic field gradient deviates more significantly in regions farther from $x = 0$. Therefore, to achieve recombination of the c.o.m trajectories in both position and momentum space, the current magnitude I must be fine-tuned to obtain an appropriate value for η_2 . As shown in the example Fig. 6 (a), in stage-3 the spin up and down trajectories gradually get closer to each other and eventually overlap at the moment τ_3 . The example given above shows the creation of a spatial superposition of a nanodiamond with mass $m = 10^{-19}$ kg. In plot Fig. 6(c), one can see that the device is capable of creating $\sim 12 \mu\text{m}$ superposition size for $m = 10^{-19}$ kg nanodiamond within less than $t = 0.1$ sec. The recombination of wave packets in the momentum space can be observed from plot Fig. 6(d).

All these three stages contribute to creating a spatial superposition, Δx , which depends on the mass, and the initial point of launch from the centre of the trapping potential, x_0 , shown in Fig. 2(a, b). In Fig. 6, we show the best possible scenario for $m = 10^{-19}$ kg nanodiamond, where we can create the largest spatial superposition of $\Delta x \sim \mathcal{O}(10 - 20) \mu\text{m}$, where we launch the nanodiamond from an initial position, $x_0 = -40 \mu\text{m}$. We also provide an analytical expression for the spatial superposition, see Eq. 26, and we plot Δx for various masses and different initial values of x_0 , see Fig. 7. As we can see, we can create a large spatial superposition of $\Delta x \sim \mathcal{O}(100) \text{ nm}$ for $m = 10^{-17} \text{ kg}$ if we start the superposition of the nanodiamond at $x_0 \sim -40 \mu\text{m}$. For heavy masses, e.g.

$m \sim 10^{-15}\text{kg}$, the superposition size remains small, i.e. $\Delta x \sim \mathcal{O}(1)\text{nm}$, even for a large initial displacement of $x_0 \sim -40\mu\text{m}$. We can see the scaling of the superposition size with regard to the mass, roughly $\Delta x \propto 1/m$ for the same values of the currents, magnetic field gradients, and x_0 . This means that for $m = 10^{-19}, 10^{-17}, 10^{-15}\text{kg}$, we get respectively, $\Delta x \sim \mathcal{O}(10)\mu\text{m}, \mathcal{O}(100)\text{nm}, \mathcal{O}(1)\text{nm}$, a hierarchy of two orders of magnitude in the superposition size when we started the superposition at $x_0 = -40\mu\text{m}$. A very similar trend continues for different initial values of x_0 .

Note that there is hardly any drift of the nanodiamond in the $y-z$ directions, as the traps are tight, and the frequencies along these directions are $\omega_y \sim \omega_z \sim 10^4\text{ Hz}$. If the nanodiamond is cooled sufficiently in $y-z$ directions, the wavepacket remains small, see footnote-3.

5. CONCLUSION AND DISCUSSION

In this work, we have proposed a chip-based apparatus for generating spatial quantum superpositions of a levitated nanodiamond. The setup comprises two functional components: a levitation assembly and a splitting assembly, each comprising four current-carrying parallel wires. The superimposed magnetic fields create approximately harmonic potentials in all three spatial dimensions. This configuration provides strong confinement in the y and z directions, while enabling the generation of a mesoscopic spatial superposition along the x -direction by applying suitable currents in the splitting wires. The superposition is maintained by applying a bias magnetic field along x , which keeps the NV centre's spin quantisation axis aligned and actively suppresses spin-flip processes. Furthermore, the functional independence of the levitation and splitting assemblies yields nearly decoupled motional degrees of freedom, thereby offering significant convenience and flexibility for precise control of the spatial superposition.

As illustrated in Fig. 1, the box-like structure of the apparatus features open ends along the $+z$ and $-z$ directions, which offers operational flexibility for the initial loading and cooling of the nanodiamond. For instance, one could incorporate an additional “Z”-wire at the bottom of the setup to efficiently cool the particle's motional state. By adjusting the corresponding bias field of this wire, the diamond could be properly initialised to the target position $(-x_0, 0, z_L)$ within our interferometric scheme. Furthermore, these open ports would provide the necessary optical or microwave access for measuring the spin state after the interferometric trajectories are recombined. In the present work, we consider an Earth-based implementation in which the balance between the diamagnetic force and gravity yields a non-zero vertical magnetic field component.

Finally, we note that all our numerical results are derived from magnetic fields generated by eight finite-length wires. A more detailed model that accounts for

the specific material properties and finite thickness of the wires would undoubtedly bring the simulations closer to real-world conditions. Nevertheless, such refinements are not expected to alter the main conclusions of this work.

In all our discussions, we have treated the nanodiamond's magnetic dipole as a point dipole, which is a very good approximation as long as the scale at which the norm of the magnetic field changes are larger than the physical dimensions of the nanoparticle, the dipole approximation holds for all magnetic field configurations considered in our paper [44]. Furthermore, note that our superposition scheme does not address the nanodiamond's libration mode. It is conceivable to stabilise all the rotational degrees of freedom by imparting an initial rotation along the NV axis, which helps to gyroscopically stabilise the nanodiamond as shown in Refs. [54, 65]. In the subsequent papers, we will consider both the effects of magnetic noise following [66, 67], and the rotational effects of nanodiamond.

acknowledgments

QX will thank Run Zhou for extensive discussions. AG is supported in part by NSF grants PHY- PHY-2409472 and PHY-2111544, the Heising-Simons Foundation, the W.M. Keck Foundation, the John Templeton Foundation, DARPA, and ONR Grant N00014-18-1-2370. SB's work is supported by an EPSRC grant EP/X009467/1. AG, SB, and AM's research is funded by the Gordon and Betty Moore Foundation through Grant GBMF12328, DOI 10.37807/GBMF12328. This material is based on work supported by the Alfred P. Sloan Foundation under Grant No. G-2023-21130.

6. APPENDICES

A. MAGNETIC FIELD

Considering that the four wires of the levitation assembly in Fig. 1 are in very close proximity to the diamond particle, when numerically calculating the magnetic field they generate, we account for both their width and thickness, i.e., their extension in the z - and y -direction, respectively. In the main text, we assume these wires carry a current of 24 A and have identical width and thickness, both of $w = 10\mu\text{m}$. It should be noted that this is a very high current density, which relies on the future development of better high-temperature superconducting materials. As a theoretical study, we use this configuration to achieve a smaller B_z , ensuring that the NV-center primarily couples with B_x . The calculation of the magnetic field generated by a wire with a quadrilateral cross-section is relatively straightforward, see for example, [62]. Here we provide a brief description.

TABLE II: Positions and currents of the levitation wires.

k	(y_k, z_k) position	current
$k = 1$	(a, b)	$I_{L,1} = -I_L$
$k = 2$	$(-a, b)$	$I_{L,2} = I_L$
$k = 3$	$(-a, -b)$	$I_{L,3} = -I_L$
$k = 4$	$(a, -b)$	$I_{L,4} = I_L$

y -component of levitation assembly:

$$\mathbf{B}_L \cdot \mathbf{e}_y = \sum_{k=1}^{k=4} \int_{z_k - \frac{w}{2}}^{z_k + \frac{w}{2}} \int_{y_k - \frac{w}{2}}^{y_k + \frac{w}{2}} f_k(y_s, z_s) dy_s dz_s \quad (28)$$

$$f_k = -\frac{\mu_0 J_k}{2\pi} \frac{(z - z_s)}{(y - y_s)^2 + (z - z_s)^2} \quad (29)$$

z -component of levitation assembly:

$$\mathbf{B}_L \cdot \mathbf{e}_z = \sum_{k=1}^{k=4} \int_{z_k - \frac{w}{2}}^{z_k + \frac{w}{2}} \int_{y_k - \frac{w}{2}}^{y_k + \frac{w}{2}} g_k(y_s, z_s) dy_s dz_s \quad (30)$$

$$g_k = \frac{\mu_0 J_k}{2\pi} \frac{(y - y_s)}{(y - y_s)^2 + (z - z_s)^2} \quad (31)$$

In the expressions above, Eqs. (29, 31) represent the simplest expressions for the y - and z -components of the magnetic field generated by an infinitely thin wire, with the original current replaced by the current density $J = I_L/w^2$. Here, (y, z) denotes the field point, (y_s, z_s) denotes arbitrary source point on the wire cross-section where we define the centre point of k^{th} wire to be (y_k, z_k) , and the subscript k indicates the specific wire number as listed in Tab. II. Therefore, after summing up contributions from all four wires, y - and z -components of the levitation assembly are derived in Eqs. (28, 30).

For the four wires of the separation assembly, recall that their mutual separation is $2L = 400 \mu\text{m}$ as shown in Fig. 1. Therefore, we directly adopt the simplest infinitely thin wire model to calculate their magnetic field components, which are given as follows: x -component:

TABLE III: Positions and currents of the separation wires.

k	(x_k, y_k) position	current
$k = 1$	(L, L)	$I_1 = -I$
$k = 2$	$(-L, L)$	$I_2 = I$
$k = 3$	$(-L, -L)$	$I_3 = -I$
$k = 4$	$(L, -L)$	$I_4 = I$

$$\mathbf{B}_S \cdot \mathbf{e}_x = \quad (32)$$

$$-\frac{\mu_0 I_{S,k}}{4\pi} \frac{y - y_k}{R_{S,k}^2} \left[\frac{z + z_s}{\sqrt{(z + z_s)^2 + R_{S,k}^2}} \right]_{z_s=-l}^{z_s=l} \quad (33)$$

y -component:

$$\mathbf{B}_S \cdot \mathbf{e}_y = \quad (34)$$

$$\frac{\mu_0 I_{S,k}}{4\pi} \frac{x - x_k}{R_{S,k}^2} \left[\frac{z + z_s}{\sqrt{(z + z_s)^2 + R_{S,k}^2}} \right]_{z_s=-l}^{z_s=l} \quad (35)$$

Similarly, I_k denotes the current magnitude in each of these four wires, where $k = 1, 2, 3, 4$ serves as a dummy index. The coordinates (x_k, y_k) represent both the position of the wire in the x - y plane and the location of the source point. $R_{S,k} = \sqrt{(x - x_k)^2 + (y - y_k)^2}$ corresponds to the shortest distance from the field point (x, y) to the wire positioned at (x_k, y_k) . Position of these four wires in the (x, y) plane is given in Tab. III. Regarding the lengths of these wires, denoted as $2l$, since all eight wires can extend freely along their longitudinal direction, this value can be set arbitrarily. In our numerical calculations, we have selected $2l = 400 \mu\text{m}$.

A.1. Magnetic levitation & confinement

Considering the magnetic field Eqs. (4), (2) and (3), we aim to create the magnitude of the field, which can be written as,

$$B(x, y, z) := |\mathbf{B}| = \sqrt{\mathbf{B}_L^2(y, z) + \mathbf{B}_S^2(x, z)} \quad (36)$$

$$= \sqrt{(\eta_S x + B_0)^2 + (\eta_L^2 z^2) + (\eta_L + \eta_S)^2 y^2},$$

Substituting this magnetic field into the diamagnetic term of Eq. (1) reveals that this form of linear magnetic field creates mutually uncoupled harmonic oscillator potentials along the x , y , and z directions. For y and z direction, the diamagnetic forces are,

$$F_L = -\partial_z \frac{\chi_\rho m}{2\mu_0} \mathbf{B}^2 = \frac{\chi_\rho m}{\mu_0} \eta_L^2 z = -m\omega_z^2 z \quad (37)$$

$$F_y = -\partial_y \frac{\chi_\rho m}{2\mu_0} \mathbf{B}^2 = \frac{\chi_\rho m}{\mu_0} (\eta_L + \eta_S)^2 y = -m\omega_y^2 y \quad (38)$$

Here, F_L represents the levitation force along the positive z -direction that balances gravity, while F_y denotes the diamagnetic restoring force in the y -direction. The frequencies ω_y and ω_z correspond to those defined in Eqs. (6) and (8), respectively. It is evident that, in the absence of gravity, both forces act to confine the particle along the central axis $(x, 0, 0)$. When $z < 0$, F_L offers a positive force against gravity as shown in Fig. 3(c).

For the target magnetic field Eqs. (4, 2, 3), we plan to employ four wires to generate it, taking the levitation assembly as an example. For the four infinitely long straight wires parallel to the x -axis that we consider, they form a rectangle in the y - z plane (see Fig. 1), with any two adjacent wires carrying currents in opposite directions. In this configuration, in the vicinity of the geometric central axis of the levitation assembly, the four

wires can only produce magnetic field components along the y and z direction,

$$B_{L,z} = \frac{\mu_0}{2\pi} \sum_{k=1}^4 \frac{(y - y_k) I_{L,k}}{(y - y_k)^2 + (z - z_k)^2} \quad (39)$$

$$B_{L,y} = \frac{\mu_0}{2\pi} \sum_{k=1}^4 \frac{-(z - z_k) I_{L,k}}{(y - y_k)^2 + (z - z_k)^2} \quad (40)$$

where k indicates four wires placed at different places in the $y - z$ plane with current $I_{L,k}$.

The magnetic field of the levitation assembly is the superposition of the eight components mentioned above (note that, for ease of discussion, we present only the results for infinitely long straight wires here). From Eqs. (38) and (37), it can be seen that the diamond will be confined near the geometric central axis $(x, 0, 0)$ (when gravity is considered, the levitation height of the diamond is close to zero, see Fig. 3(c)). Therefore, we can perform a Taylor expansion of Eqs. (39, 40) around $(x, 0, 0)$, summing up the contribution from each wire to obtain the gradient expressions,

$$\begin{aligned} \frac{\partial B_{L,z}}{\partial z} \Big|_{(0,0)} &= -\frac{\mu_0}{\pi} \sum_{k=1}^4 \frac{y_k z_k}{(y_k^2 + z_k^2)^2} I_{L,k} \\ &= \frac{4\mu_0}{\pi} \frac{ab}{(a^2 + b^2)^2} I_L \end{aligned} \quad (41)$$

One can find that taking the partial derivative of Eq. (40) with respect to y yields a magnetic field gradient identical to that of Eq. (41), differing only in sign.

Similarly, one can estimate the magnetic field gradient of the separation assembly in the vicinity of the geometric centre of the setup using the infinitely long wire model. For our specific parameters, the magnetic field components of the separation assembly can be expressed in the following form,

$$B_{S,x} = \frac{\mu_0}{2\pi} \sum_{k=1}^4 \frac{-(y - y_k) I_k}{(x - x_k)^2 + (y - y_k)^2} \quad (42)$$

$$B_{S,y} = \frac{\mu_0}{2\pi} \sum_{k=1}^4 \frac{(x - x_k) I_k}{(x - x_k)^2 + (y - y_k)^2} \quad (43)$$

where k indicates four wires placed at different places in the $x - y$ plane with current I_k .

Similarly, one can perform a Taylor expansion around the geometric centre of the setup at $(0, 0, z)$ to obtain the expression for the magnetic field gradient in the x - y plane.

$$\begin{aligned} \frac{\partial B_{S,x}}{\partial x} \Big|_{(0,0)} &= \frac{\mu_0}{\pi} \sum_{k=1}^4 \frac{x_k y_k}{(x_k^2 + y_k^2)^2} I_k \\ &= -\frac{\mu_0}{\pi} \frac{I}{L^2} \end{aligned} \quad (44)$$

Note that this result should be used for estimation purposes only, because the scale of the particle's motion in the x -direction is large (though still smaller than $2L$).

B. PROTOCOL

B.1. Stage-1

In the separation stage, the magnetic field is given by Eq. (13), the potential regarding diamond's x -motion can be written as,

$$U(x, z_L) = -\frac{\chi_\rho m}{2\mu_0} \mathbf{B}^2(x, z_L) + \hbar\gamma_e S_x B_x(x, z_L). \quad (45)$$

The equation of motion is then,

$$\begin{aligned} \frac{d^2 x}{dt^2} &= -\frac{\chi_\rho}{\mu_0} \eta_1^2 x - \left(\frac{\chi_\rho B_0}{\mu_0} - \frac{\hbar\gamma_e S_x}{m} \right) \eta_1 \\ &= -\omega_1^2 x - \left(\frac{\chi_\rho B_0}{\mu_0} - \frac{\hbar\gamma_e S_x}{m} \right) \eta_1. \end{aligned} \quad (46)$$

The solution can be solved as,

$$x_1^\pm(t) = (-x_0 - k_1^\pm) \cos \omega_1 t + k_1^\pm \quad (47)$$

$$\dot{x}_1^\pm(t) = \omega_1(x_0 + k_1^\pm) \sin \omega_1 t, \quad (48)$$

where we define $k_1^\pm = k_1(S_x) = \frac{1}{\eta_1} \left(B_0 - \frac{\mu_0 \hbar \gamma_e S_x}{m \chi_\rho} \right)$. Therefore, here are two trajectories corresponding to spin-up and spin-down, respectively. $-x_0 < 0$ is the initial position of stage-1 which suggest that both wave packets will go to the positive side of x -axis. The separation in this stage can be written as,

$$\begin{aligned} \Delta x_1(t) &= x_1^+(t) - x_1^-(t) \\ &= -\Delta k_1 \cos \omega_1 t + \Delta k_1, \end{aligned} \quad (49)$$

where we define,

$$\Delta k_1 = k_1^+ - k_1^- = -2 \frac{\mu_0 \hbar \gamma_e}{\eta_1 m \chi_\rho}, \quad (50)$$

which is a positive value. Eqs. (49) and (50) indicate that as the experiment proceeds, the spatial superposition of the wave packets begins to expand and $\Delta x_1 > 0$. Here, we choose to define the ending moment τ_1 of this stage based on the geometric centre of the two wave packets. The geometric centre of the two wave packets corresponds to a virtual trajectory with zero spin. We choose to end this stage when this trajectory with $S_x = 0$ reaches $x = 0$.

$$\tau_1 = \frac{1}{\omega_1} \arccos \left(\frac{B_0}{\eta_1 x_0 + B_0} \right). \quad (51)$$

Due to our configuration of B_0 , in the vicinity of $x = 0$, the $B_x(x^\pm(t), z_L)$ experienced by the two trajectories is always much greater than $B_z(y \approx 0, z_L)$. Therefore, there is considerable freedom in selecting the ending moment for the first stage. Our choices for the initial position $-x_0$ and the final moment in this stage aim to fully utilise the linear magnetic-field region created by the splitting device.

B.2. Stage-2

In the second stage, we map the magnetic field from Eq. (13) to Eq. (14). The only difference between the magnetic field in this stage and that in Stage-1 is that the gradient of the magnetic field is reversed ($-\eta_1 \rightarrow \eta_1$). This operation corresponds to reversing the current I in the splitting device. At the moment τ_1 , substitute Eq. (51) into Eqs. (47, 48). The positions and velocities are,

$$\begin{aligned} X_1^\pm &= -\frac{1}{\chi_\rho m} \frac{\hbar \gamma_e S_x \mu_0 x_0}{B_0 + \eta_1 x_0} \\ \dot{X}_1^\pm &= \omega_1 (k_1^\pm + x_0) \sqrt{\frac{x_0^2 \eta_1^2 + 2B_0 x_0 \eta_1}{(B_0 + x_0 \eta_1)^2}} \end{aligned} \quad (52)$$

The potential and dynamics are essentially the same as Eqs. (45, 46) with different gradient and initial conditions. Trajectories in the stage-2 can be written as

$$\begin{aligned} x_2^\pm(t) &= (X_1^\pm + k_1^\pm) \cos [\omega_1(t - \tau_1)] - k_1^\pm \\ &\quad + \frac{\dot{X}_1^\pm}{\omega_1} \sin [\omega_1(t - \tau_1)] \end{aligned} \quad (53)$$

The size of the superposition in this stage is then,

$$\begin{aligned} \Delta x_2(t) &= (\Delta X_1 + \Delta k_1) \cos [\omega_1(t - \tau_1)] - \Delta k_1 \\ &\quad + \frac{\Delta \dot{X}_1}{\omega_1} \sin [\omega_1(t - \tau_1)] \\ &= R \sin [\omega_1(t - \tau_1) + \phi] - \Delta k_1, \end{aligned} \quad (54)$$

where,

$$\begin{aligned} R &= \sqrt{\left(\frac{\Delta \dot{X}_1}{\omega_1}\right)^2 + (\Delta X_1 + \Delta k_1)^2} \\ \phi &= \arctan \left[\frac{\omega_1 (\Delta X_1 + \Delta k_1)}{\Delta \dot{X}_1} \right]. \end{aligned} \quad (55)$$

Similar to the trajectories, the superposition size Eq. (54) in this stage continues to increase, at the moment,

$$t_{\max} = \frac{\pi - 2\phi}{2\omega_1} + \tau_1, \quad (56)$$

The size is maximised where the duration of this stage is $T_2 = \frac{\pi - 2\phi}{2\omega_1}$. After this moment, the size begins to decrease, hence closing. And, the trajectories will also reach to corresponding maximums and begin to “fall” back to $x = 0$ axis, with minus velocities. The recombination of the trajectories in position and momentum basis does not occur in this stage. The duration T_2 of this stage can be chosen arbitrarily. Here, we choose the ending moment as

$$\tau_2 = \frac{\pi - 2\phi}{\omega_1} + \tau_1. \quad (57)$$

At the chosen ending moment, the separation between the two trajectories will return to the initial separation $\Delta x_2(\tau_1)$. It should be noted that the final positions X_2^\pm and velocities \dot{X}_2^\pm of the spin-up and spin-down trajectories at the end of this stage do not necessarily need to be symmetric with those of the first stage.

B.3. Stage-3

At the beginning of the recombination stage, the current in the splitting device is reversed and with a different current strength. As mentioned in the closing stage, the final positions X_2^\pm and velocities \dot{X}_2^\pm do not necessarily need to be symmetric with X_1^\pm and \dot{X}_1^\pm . Therefore, the gradient magnitude η_2 used for recombine the trajectories both in position and momentum basis will be different from η_1 . In this stage, the field is mapped to Eq. (15) and the solutions can be written as

$$\begin{aligned} x_3^\pm(t) &= (k_2^\pm - X_2^\pm) \cos [\omega_2(t - \tau_2)] \\ &\quad + k_2^\pm + \frac{\dot{X}_2^\pm}{\omega_2} \sin [\omega_2(t - \tau_2)], \end{aligned} \quad (58)$$

likewise we define $k_2^\pm = k_2(S_x) = \frac{1}{\eta_2} \left(B_0 - \frac{\mu_0 \gamma_e \hbar S_x}{m \chi_\rho} \right)$. The difference is

$$\begin{aligned} \Delta x_3(t) &= -(\Delta k_2 - \Delta X_2) \cos [\omega_2(t - \tau_2)] + \Delta k_2 \\ &\quad + \frac{\Delta \dot{X}_2}{\omega_2} \sin [\omega_2(t - \tau_2)] \\ &= R_2 \sin [\omega_2(t - \tau_2) + \phi_2] + \Delta k_2, \end{aligned} \quad (59)$$

where,

$$\begin{aligned} R_2 &= \sqrt{\left(\frac{\Delta \dot{X}_2}{\omega_2}\right)^2 + (\Delta X_2 - \Delta k_2)^2} \\ \phi_2 &= \arctan \left[\frac{\omega_2 (\Delta X_2 - \Delta k_2)}{\Delta \dot{X}_2} \right]. \end{aligned} \quad (60)$$

[1] S. Bose, A. Mazumdar, G. W. Morley, H. Ulbricht, M. Toroš, M. Paternostro, A. Geraci, P. Barker, M. S. Kim, and G. Milburn, *Phys. Rev. Lett.* **119**, 240401 (2017).

[2] S. Bose, https://www.youtube.com/watch?v=0Fv-0k13s_k (2016), accessed 1/11/22, on behalf of QGEM collaboration.

[3] C. Marletto and V. Vedral, *Phys. Rev. Lett.* **119**, 240402 (2017).

[4] R. Penrose, *Gen. Rel. Grav.* **28**, 581 (1996).

[5] L. Diósi, *Phys. Rev. A* **40**, 1165 (1989).

[6] P. M. Pearle, *Phys. Rev. A* **39**, 2277 (1989).

[7] A. Bassi, K. Lochan, S. Satin, T. P. Singh, and H. Ulbricht, *Rev. Mod. Phys.* **85**, 471 (2013), arXiv:1204.4325 [quant-ph].

[8] S. Nimmrichter and K. Hornberger, *Phys. Rev. Lett.* **110**, 160403 (2013).

[9] R. J. Marshman, A. Mazumdar, and S. Bose, *Phys. Rev. A* **101**, 052110 (2020).

[10] S. Bose, A. Mazumdar, M. Schut, and M. Toroš, *Phys. Rev. D* **105**, 106028 (2022).

[11] M. Christodoulou et al., (2022), arXiv:2202.03368 .

[12] D. Carney, P. C. E. Stamp, and J. M. Taylor, *Class. Quant. Grav.* **36**, 034001 (2019).

[13] D. L. Danielson, G. Satishchandran, and R. M. Wald, *Phys. Rev. D* **105**, 086001 (2022).

[14] U. K. B. Vinckers, A. de la Cruz-Dombriz, and A. Mazumdar, *Phys. Rev. D* **107**, 124036 (2023), arXiv:2303.17640 [gr-qc] .

[15] S. G. Elahi and A. Mazumdar, *Phys. Rev. D* **108**, 035018 (2023), arXiv:2303.07371 [gr-qc] .

[16] S. Bose, A. Mazumdar, M. Schut, and M. Toroš, *Entropy* **25**, 448 (2023), arXiv:2203.11628 [gr-qc] .

[17] S. Chakraborty, A. Mazumdar, and R. Pradhan, *Phys. Rev. D* **108**, L121505 (2023), arXiv:2310.06899 [gr-qc] .

[18] M. Toroš, M. Schut, P. Andriolo, S. Bose, and A. Mazumdar, *Phys. Rev. D* **111**, 036026 (2025), arXiv:2405.04661 [quant-ph] .

[19] P. F. Barker, S. Bose, R. J. Marshman, and A. Mazumdar, *Phys. Rev. D* **106**, L041901 (2022), arXiv:2203.00038 [hep-ph] .

[20] D. Biswas, S. Bose, A. Mazumdar, and M. Toroš, *Phys. Rev. D* **108**, 064023 (2023), arXiv:2209.09273 [gr-qc] .

[21] J. Tilly, R. J. Marshman, A. Mazumdar, and S. Bose, *Phys. Rev. A* **104**, 052416 (2021).

[22] T. W. van de Kamp, R. J. Marshman, S. Bose, and A. Mazumdar, *Phys. Rev. A* **102**, 062807 (2020).

[23] H. Chevalier, A. J. Paige, and M. S. Kim, *Phys. Rev. A* **102**, 022428 (2020).

[24] M. Schut, A. Geraci, S. Bose, and A. Mazumdar, *Phys. Rev. Res.* **6**, 013199 (2024), arXiv:2307.15743 [quant-ph] .

[25] M. Schut and A. Mazumdar, (2025), arXiv:2502.12474 [quant-ph] .

[26] J.-F. Hsu, P. Ji, C. W. Lewandowski, and B. D'Urso, *Sci. Rep.* **6**, 30125 (2016).

[27] C. Wan, M. Scala, G. Morley, A. Rahman, H. Ulbricht, J. Bateman, P. Barker, S. Bose, and M. Kim, *Phys. Rev. Lett.* **117**, 143003 (2016).

[28] M. Scala, M. S. Kim, G. W. Morley, P. F. Barker, and S. Bose, *Phys. Rev. Lett.* **111**, 180403 (2013).

[29] R. J. Marshman, A. Mazumdar, G. W. Morley, P. F. Barker, S. Hoekstra, and S. Bose, *New J. Phys.* **22**, 083012 (2020), arXiv:1807.10830 [gr-qc] .

[30] R. J. Marshman, A. Mazumdar, R. Folman, and S. Bose, *Phys. Rev. Res.* **4**, 023087 (2022), arXiv:2105.01094 [quant-ph] .

[31] J. S. Pedernales, G. W. Morley, and M. B. Plenio, *Physical review letters* **125**, 023602 (2020).

[32] R. Zhou, R. J. Marshman, S. Bose, and A. Mazumdar, *Phys. Rev. Res.* **4**, 043157 (2022).

[33] R. Zhou, R. J. Marshman, S. Bose, and A. Mazumdar, *Phys. Rev. A* **107**, 032212 (2023), arXiv:2210.05689 [quant-ph] .

[34] R. Zhou, R. J. Marshman, S. Bose, and A. Mazumdar, *Phys. Scripta* **99**, 055114 (2024), arXiv:2211.08435 [quant-ph] .

[35] R. Zhou, Q. Xiang, and A. Mazumdar, *Phys. Rev. A* **111**, 052207 (2025), arXiv:2408.11909 [quant-ph] .

[36] O. Amit, Y. Margalit, O. Dobkowski, Z. Zhou, Y. Japha, M. Zimmermann, M. A. Efremov, F. A. Narducci, E. M. Rasel, W. P. Schleich, and R. Folman, *Phys. Rev. Lett.* **123**, 083601 (2019).

[37] S. Machluf, Y. Japha, and R. Folman, *Nature Communications* **4**, 2424 (2013).

[38] Y. Margalit, Z. Zhou, O. Dobkowski, Y. Japha, D. Rohrlich, S. Moukouri, and R. Folman, arXiv preprint arXiv:1801.02708 (2018).

[39] O. Amit, Y. Margalit, O. Dobkowski, Z. Zhou, Y. Japha, M. Zimmermann, M. A. Efremov, F. A. Narducci, E. M. Rasel, W. P. Schleich, and R. Folman, *Physical Review Letters* **123**, 083601 (2019).

[40] Y. Margalit et al., (2020), 10.1126/sciadv.abg2879, arXiv:2011.10928 [quant-ph] .

[41] M. Keil, S. Machluf, Y. Margalit, Z. Zhou, O. Amit, O. Dobkowski, Y. Japha, S. Moukouri, D. Rohrlich, Z. Binstock, Y. Bar-Haim, M. Givon, D. Groswasser, Y. Meir, and R. Folman, “Stern-Gerlach interferometry with the atom chip,” in *Molecular Beams in Physics and Chemistry* (Springer International Publishing, 2021) p. 263–301.

[42] S. Machluf, Y. Japha, and R. Folman, *Nature communications* **4**, 2424 (2013).

[43] R. Folman, P. Krüger, D. Cassettari, B. Hessmo, T. Maier, and J. Schmiedmayer, *Phys. Rev. Lett.* **84**, 4749 (2000).

[44] S. G. Elahi, M. Schut, A. Dana, A. Grinin, S. Bose, A. Mazumdar, and A. Geraci, *Phys. Rev. A* **112**, 063508 (2025), arXiv:2411.02325 [quant-ph] .

[45] S. Gupta, D. S. Bykov, T. E. Northup, and C. Gonzalez-Ballester, (2025), arXiv:2511.21495 [quant-ph] .

[46] L. Dania, D. S. Bykov, F. Goschin, M. Teller, A. Kassid, and T. E. Northup, *Phys. Rev. Lett.* **132**, 133602 (2024).

[47] L. Dania, D. S. Bykov, M. Knoll, P. Mestres, and T. E. Northup, *Phys. Rev. Res.* **3**, 013018 (2021).

[48] L. Dania, K. Heidegger, D. S. Bykov, G. Cerchiari, G. Araneda, and T. E. Northup, *Phys. Rev. Lett.* **129**, 013601 (2022).

[49] M. Muretova, Y. Japha, M. Toros, and R. Folman, (2025), arXiv:2508.13723 [quant-ph] .

[50] J. Pérez-Ríos and A. Sanz, *American Journal of Physics* **81**, 836 (2013).

- [51] J. Reichel and V. Vuletic, Atom chips (John Wiley & Sons, 2011).
- [52] Y. Japha and R. Folman, *Physical Review Letters* **130**, 113602 (2023), arxiv:2202.10535 [quant-ph] .
- [53] Y. Japha and R. Folman, (2022), 10.48550/arxiv.2202.10535.
- [54] R. Rizaldy, T. Zhou, S. Bose, and A. Mazumdar, *Phys. Rev. Res.* **7**, 043095 (2025), arXiv:2412.15335 [quant-ph] .
- [55] J. Heremans, C. H. Olk, and D. T. Morelli, *Phys. Rev. B* **49**, 15122 (1994).
- [56] E. Tiesinga, P. J. Mohr, D. B. Newell, and B. N. Taylor, *Journal of physical and chemical reference data* **50** (2021).
- [57] M. Toroš, T. W. Van De Kamp, R. J. Marshman, M. S. Kim, A. Mazumdar, and S. Bose, *Phys. Rev. Res.* **3**, 023178 (2021).
- [58] M.-Z. Wu, (2024), arXiv:2406.10832 [quant-ph] .
- [59] M.-Z. Wu, M. Toroš, S. Bose, and A. Mazumdar, *Phys. Rev. D* **111**, 064004 (2025), arXiv:2404.15455 [quant-ph] .
- [60] M.-Z. Wu, M. Toroš, S. Bose, and A. Mazumdar, *Phys. Rev. D* **112**, 062006 (2025), arXiv:2507.00280 [quant-ph] .
- [61] M.-Z. Wu, arXiv preprint arXiv:2406.10832 (2024).
- [62] W. K. Panofsky and M. Phillips, Classical electricity and magnetism (Courier Corporation, 2012).
- [63] C. Montoya, J. Valencia, A. A. Geraci, M. Eardley, J. Moreland, L. Hollberg, and J. Kitching, *Physical Review A* **91**, 063835 (2015).
- [64] F. P. Incropera, D. P. DeWitt, T. L. Bergman, A. S. Lavine, et al., Fundamentals of heat and mass transfer, Vol. 6 (Wiley New York, 1996).
- [65] T. Zhou, S. Bose, and A. Mazumdar, *Phys. Rev. A* **112**, 013315 (2025), arXiv:2407.15813 [quant-ph] .
- [66] S. N. Moorthy, A. Geraci, S. Bose, and A. Mazumdar, *Phys. Rev. A* **112**, 022416 (2025), arXiv:2504.13252 [quant-ph] .
- [67] S. N. Moorthy and A. Mazumdar, (2025), arXiv:2509.02670 [quant-ph] .